IEEE Access
Multidisciplinary | Rapid Review | Open Access Journal

Date of publication xxxx 00, 0000, date of current version xxxx 00, 0000.

Digital Object Identifier 10.1109/ACCESS.2017.Doi Number

Extraction of Flux Leakage and Eddy Current Signals Induced by Submillimeter Backside Slits on Carbon Steel Plate using A Low-Field AMR Differential Magnetic Probe

Mohd Aufa Hadi Putera Zaini[1], Mohd Mawardi Saari[1,2], (Member, IEEE), Nurul A'in Nadzri[1], Zulkifly Aziz[1], Nur Huda Ramlan[3], and Keiji Tsukada[4]

[1]Faculty of Electrical and Electronic Engineering Technology, Universiti Malaysia Pahang, Pekan Campus, Pekan 26600, Malaysia
[2]Centre for Sensor Technology, Universiti Malaysia Pahang, Pekan 26600, Malaysia
[3]College of Engineering, Universiti Malaysia Pahang, Kuantan 26300, Malaysia
[4]Graduate School of Interdisciplinary Science and Engineering in Health Systems, Okayama University, Okayama 700-8530, Japan

Corresponding author: Mohd Mawardi Saari (e-mail: mmawardi@ump.edu.my).

The authors would like to thank the Ministry of Higher Education for providing financial support under Fundamental Research Grant Scheme (FRGS) No. FRGS/1/2019/TK04/UMP/02/4 (University reference RDU1901154) and Universiti Malaysia Pahang for laboratory facilities as well as additional financial support under Internal Research grant RDU1903100. A special thank you to Dr. Aiman Mohd Halil on behalf of the Faculty of Mechanical and Automotive Engineering Technology, Universiti Malaysia Pahang, for his contributions toward this research.

ABSTRACT Magnetic Flux Leakage (MFL) and Eddy Current Testing (ECT) are commonly employed as the non-destructive evaluation (NDE) techniques used to detect defects within the steel. The MFL technique is advantageous in terms of deep defects detection, while the ECT technique excels in providing dense information regarding defects. In this work, artificial MFL and eddy current (EC) signals in ferromagnetic materials are studied, and an experimental magnetic probe that utilizes both techniques is developed for signal verification. The separation between MFL and EC signals is achieved by utilizing the phase-sensitive detection technique, implementing a dynamic referencing method as opposed to the conventional static phase referencing. A finite element method (FEM) based simulation is employed to study and verify the MFL and EC signals measured by the proposed magnetic probe. The proposed magnetic probe features highly sensitive anisotropic magneto-resistive sensors capable of measuring the MFL and EC signals induced by artificial slits of varying depths engraved onto a 2-mm carbon steel plate. Finite element simulations indicate different flux leakage patterns and eddy current signals detected in the vicinity of the back-side slits. A good agreement is observed between the simulated and the measured MFL and EC signals for the optimized frequency range of 110-210 Hz with the corresponding Lissajous curve for the detection of submillimeter back-side slits. The study has shown that the combination of MFL and EC signals can be successfully captured by an appropriate magnetic probe for an enhanced detection performance of back-side defects in ferromagnetic materials.

INDEX TERMS anisotropy magnetoresistance, AMR, eddy current testing, ECT, finite element modeling, FEM, magnetic flux leakage, MFL, phase-sensitive detection, slit detection, steel.

I. INTRODUCTION

Steel is widely known as one of the key materials required for the construction of numerous infrastructures such as highways, trains, and buildings. Owing to its versatility, steel appears in countless forms, from cables to reinforcement plates for large structures such as buildings and bridges [1].

When defects occur within the steel structure, its integrity is compromised, thus risking an infrastructure collapse. This catastrophic failure may cost lives. Therefore, early detection of surface defects is considered a critical preventive measure. Corrosion and metal loss are the two most prominent reasons leading to crack defects. In addition, shrinkage and segregation during the cooling period of the welding process

may also contribute to the formation of cracks [2], [3]. Typical cracks usually progress from tiny (e.g., micron-sized/nanometer-sized) hairline fracture until it becomes large enough to affect the integrity of the steel structures. Therefore, the early detection of crack development within the steel structures is essential.

Non-destructive evaluation (NDE) has been proven to be extremely effective in providing real-time inspection of defects. The techniques of NDE can be divided into several profiles, such as visual inspection [1], [4], [5], radiography [6], [7], ultrasonic [8], [9], and magnetic [10]–[13]. An emerging measurement technique based on magnetic field disturbance in the presence of defects is considered a high potential for early detection of cracks within a steel structure, owing to steel's conductive and ferromagnetic characteristics. Not only that, the safe, rapid, and non-contact nature of the magnetic field measurement technique further justify the convenience of using this method [14], [15].

The magnetic field measurement methods can generally be classified into several techniques which utilize either the principle of flux leakage measurement or eddy current measurement [16], [17]. The flux leakage measurement refers to the study of magnetic flux that simply 'leaks' out of the sample in the vicinity of cracks, whereas the eddy current measurement is the study of eddy currents that are induced when a conductive sample is exposed to an external magnetic field. Some of the techniques that utilize the principle of flux leakage measurement are Magnetic Particle Inspection (MPI) [18], [19] and Magnetic Flux Leakage (MFL) [16], [20]. MFL has been shown to be able to detect deep defects in thick ferromagnetic plates. A study based on deep defect detection within a 12-mm plate has been conducted and identified using a measurement system that incorporates a magnetic yoke, GMR sensor, and a selective amplifier [21]. Besides that, by utilizing the finite element method (FEM), the capability of the MFL technique in detecting deep defects can be further demonstrated. In addition, the relevance of 2D modeling for this technique is also highlighted [22], [23].

However, the conventional MFL method requires a high-power current source to saturate a ferromagnetic sample by producing a strong magnetic field within the constant region of the B-H curve. Although the production of strong flux leakages is possible, the practicality of using the high-power current source may be limited in certain applications, such as when a mobile measurement is required and a long operating time is necessary. In order to address this issue, a method of using a highly sensitive sensor has been proposed in [16] where weak flux leakage can be detected without having to saturate the ferromagnetic sample.

On the other hand, eddy current testing (ECT) [24], [25], pulsed eddy current (PEC) [26], remote field eddy current testing (RFECT) [13], and alternating current field measurement (ACFM) [27] are based on the principle of eddy current measurement. Techniques based on eddy current measurement have shown relatively good performance in characterizing the defect's dimension and orientation. Cheng et al. [28] examined the defect of wall-thinning within carbon steel pipes by using the PEC technique. The developed eddy current probe, which utilizes differential AMR sensors, was able to measure magnetic field with a magnitude as low as micro-Gauss. This clearly showed the capability of the AMR sensors in detecting a small-sized defect, making it a preferable choice for inspecting a small-scale defect within inner pipes. By utilizing an array of GMR sensors for the ECT probe, Vacher et al. [29] were able to detect deep small-sized defects with a size of less than 100 μm thickness on a 7-mm stainless steel pipe.

In conventional applications, the ECT is rarely applied to ferromagnetic materials due to the production of a strong background magnetization signal after exposure towards an external magnetic field and shallow penetration depth of the electromagnetic wave due to the high magnetic permeability of the materials. The effect will complicate the eddy current analysis caused by the presence of a background magnetization signal. This will limit the applicability of the conventional eddy current probes since most of them use induction coils to detect eddy current-induced magnetic fields. In addition, there will be a tradeoff between sensitivity and penetration depth, as increasing the excitation frequency will increase the probe's sensitivity at the expense of lower penetration depth. Thus, it will limit the reliability in detecting deep defects if such probes are used.

Two types of magnetic signals are induced when a ferromagnetic steel sample is exposed to an AC magnetic field, which are the strong magnetization signal and the weak eddy current signal. Conventionally, to separate these signals based on their phase property, the excitation current is used as the reference signal in the phase-sensitive detection. This signal separation technique relies on the static phase information of the excitation current where the in-phase and out-of-phase components are related to the magnetization and eddy current signals, respectively. In the case where a magnetic property distribution such as magnetic permeability exists over a ferromagnetic sample, their phase property will be varied according to the magnetic property distribution, i.e., variation in the electromagnetic propagation delay within the sample. This variation will lead to a poor separation between the magnetization and eddy current signals when a static phase reference is used, and the weak eddy current signal may still be buried within the strong magnetization signal. Therefore, a phase-sensitive detection technique that is insensitive to the variation of the magnetic property distribution is crucial for a robust separation between these signals.

This research is focused on validating the magnetic flux leakage and eddy current signals and applying both the MFL and ECT techniques for the detection of back-side slits on a carbon steel plate. Since the carbon steel plate is both ferromagnetic and conductive in nature, it will allow both

MFL and eddy current signals to be induced within the plate concurrently. Therefore, simultaneous application of the MFL and ECT techniques can be expected to hybridize both techniques' advantages, such as deep defect detection of the MFL technique and richer information in defect's dimension and orientation of the ECT technique. Firstly, the FEM simulation is conducted for the 2D model to characterize the magnetic flux leakage and eddy current signals for the proposed magnetic probe design. A phase-sensitive detection technique is proposed in an attempt to sensitively separate the eddy current and magnetization signals. Then, a differential magnetic probe with the same feature is fabricated by using the AMR sensors. The differential configuration is used in the probe design so that the environmental magnetic noise can be reduced effectively while detecting the eddy current distribution that is perpendicular to the differential direction of the AMR sensors based on Hosaka-Cohen transformation.

In the simulation work, carbon steel plates with variable thicknesses and identical back-side slits are used as the sample. A 2-mm carbon steel plate is used in the experimental work, where artificial slits with the same width and length but vary in depth are fabricated on the plate. In the simulation and experimental works, the relationship between the magnetic flux leakage and eddy current signals with the depth of the slits is further analyzed.

II. Methodology

A. SIMULATION SETUP

When a magnetic field, B_{apply} is applied to a metallic material, such as steel, eddy current will then be induced inside the said material. The induced eddy current, J_{eddy} can be represented as,

$$J_{eddy} = J_0 e^{-\sqrt{\pi f \mu \sigma} z} e^{j(2\pi f t + \alpha_0 - \sqrt{\pi f \mu \sigma} z)} \quad (1)$$

where J_0 and α_0 are the initial eddy current and phase lag at $z = 0$, while z represents the level of penetration depth whereas f μ and σ represent the frequency, the permeability of the sample, and the permittivity of the sample, respectively. Consequently, a secondary magnetic field, B_{eddy}, is also generated.

The magnetic field response emitted by the metallic material can be detected by a magnetic sensor. The detected magnetic field, B_{sensor} is made up of two components known as the magnetic flux leakage and the secondary magnetic field from the induced eddy current. Compared to the signal of the magnetic flux leakage, the eddy current signal can be considered to have a phase delay of 90° based on Faraday's Law [30], thus, allowing the signals to be separated by phase-sensitive detection technique. Both the magnetic flux leakage signal, B_{MFL} and the eddy current signal, B_{eddy} can be represented by the real and imaginary components from the following equations,

$$B_{sensor} \approx B_{MFL} + jB_{eddy}\,. \quad (2)$$

Here, B_{MFL} consists of the magnetic flux leakage from the sample and the stray magnetic field from the excitation coil, where both of the signals will be in-phase with the excitation current. The penetration depth (δ) is obtained by solving the four Maxwell's equations and is expressed as,

$$\delta = \frac{1}{\sqrt{\pi f \mu \sigma}}, \quad (3)$$

where eddy current, J_{eddy} at either *x*- or *y*-direction decays by e^{-1} or 36.8%.

To theoretically prove that eddy current and magnetization signals can be separated, a two-dimensional (2D) model was constructed for the FEM method as in Fig. 1 to validate the magnetic flux leakage and the eddy current signals using the parameters as summarized in Table 1. The 2D model consisted of two excitation coils wound around a soft iron core with a carbon steel plate as the sample. The winding in each excitation coil was set to 100 turns with a turn diameter of 6 mm, while the wire diameter was set to 0.7 mm. Initially, verification of the magnetic flux leakage and eddy current signal was simulated for a defectless sample. Two points are marked on the 2D model, where the signal was measured. Then, the measured signal at one point was subtracted from the measured signal at another point to mimic a probe in differential sensor mode. The points were represented by the red dots in Fig. 1 for the defectless sample. The points were vertically positioned at 1 mm above the sample while horizontally separated by 2 mm from the horizontal center and a spacing of 4 mm between the points. The coils' excitation current was set to 0.3 A, producing 0.42 mT.

Meanwhile, since the relative permeability of the carbon steel plate is relatively high, the excitation field should be set to less than 1 kHz compared to conventional ECT techniques. The low excitation frequency is required to enable sufficient penetration depth of the applied magnetic field within the sample [25]. The excitation frequency was varied between 10-510 Hz so that the dependency of magnetic flux leakage and eddy current signal within this frequency range could be clarified. Moreover, the direction of the excitation current in each coil was set to be in the opposite direction to each other. Furthermore, since carbon steel plates with thicknesses from 2 to 10 mm are commonly utilized in industrial applications [30], [31], elucidation of magnetic flux leakage and eddy current signal characteristics at different thicknesses should be performed. For this reason, the thickness of the samples was set to 2, 4, 6, 8, and 10 mm in the simulation, and the line scanning method was conducted for these samples.

TABLE 1
PARAMETERS FOR THE 2-D FE MODEL.

Parameters	Settings
Excitation coils	Number of coils: 2,
	Number of turns: 100,
	Diameter of coils: 6 mm,
	Diameter of wires: 0.7 mm,
	Excitation amplitude: 0.3 A,
	Excitation frequency: 10, 30, 70, 90, 110, 160, 210,
	410, and 510 Hz
Yoke	Conductivity: 10 S/m,
	Relative permeability: 3000,
	Height: 21 mm,
	Diameter: 5 mm
Sample	Conductivity: 8.41×10^6 S/m,
	Relative permeability: 129,
	Width: 80 mm,
	Height/Thickness: 2, 4, 6, 8, and 10 mm
Defect/Slit	Width: 1 mm,
	Height/Depth: 1 mm,
	Position: Backside
Mesh	Maximum element size: 1 mm,
	Minimum element size: 0.002 mm

Then, another FE model was constructed to represent the sample with defect, where a slit of depth and width of 1 mm was engraved on the back-side of the sample as in Fig. 1. To imitate the line scan measurement, both excitation coils with their cores aligned along the red dots were moved horizontally at 1-mm intervals. Their positions were varied from −15 mm to 15 mm (measured from the horizontal center), as illustrated in Fig. 1, where the differential magnetization signal, $B_{z,1}$-$B_{z,2}$ was calculated by S_1-S_2, where both S_1 and S_2 were simulated at 31 positions.

B. EXPERIMENTAL SETUP

1) AMR MAGNETIC PROBE

The magnetic probe was fabricated based on the same configuration as in the previous simulation using two excitation coils, where each coil was wound around a core as in Fig. 2. Each coil was made up of magnet wires with an internal diameter of 6 mm, and consisted of 100 turns with a strand diameter of 0.7 mm. In addition, ferrite cores having a dimension of 6 x 20 mm (diameter x height) were used for the coils. As for the sensors, two HMC1001 AMR sensors were employed with a baseline of 4 mm. Each sensor consisted of four magneto-resistive (MR) elements, where all of the MR elements were connected via a Wheatstone bridge configuration. The AMR sensor was DC-biased at 5 V. The resistivity of the MR elements would change in the presence of an applied external magnetic field due to the magneto-resistive effect and measured as a potential difference between two MR elements. Due to constraints of the AMR sensors' pin arrangement, their sensitive axis was set to the negative z-direction, measuring the B_z (normal) component of the magnetic response from the sample.

The output of the AMR sensors was then connected to an AD8249 instrumentation amplifier (INA) with a gain of 129. When a magnetic field greater than 2 Gauss was introduced to the AMR sensors, their sensitivity would be reduced drastically when the electron spins of the MR elements were trapped in the vertical position of the anisotropy axis. To reorientate the spin at 45° from the anisotropy axis, a set/reset circuit was constructed to supply high current pulses to the AMR set/reset straps. Mechanical switch (manual switching) and electronic switch (automatic switching) were embedded within the set/reset circuit to control the flow of the high pulse current. A power supply module consisting of an LM7805 voltage regulator and a TLE2426 rail splitter has been fabricated to provide low drop-out DC voltage to the AMR sensors and the INAs.

2) MEASUREMENT SETUP

In addition to the magnetic probes, the measurement setup also consisted of a DAQ card (NI-USB 6210, National Instruments), a current amplifier, a function generator, and a computer. The sampling rate was set to be 50 kS/s. Since a lock-in amplifier (LIA) can extract a signal's phase and amplitude within an extremely noisy environment by implementing the phase-sensitive detection technique, a digital type of the LIA was used for the signal extraction purpose, developed in LabVIEW (National Instruments) [32]. Compared to the analog type of LIA, the digital LIA excelled in terms of its physical size. The developed LIA was able to detect phase change and intensity change up to 50 kHz within −5 to 5 V. Furthermore, the phase and amplitude detection accuracies of the developed LIA were determined to be 0.3 % and 1%, respectively. The measurement setup was described in Fig. 2, where the measurement probe was attached to an *XY*-stage with a dimension of 55 cm (width) × 45 cm (length).

TABLE 2
THE SLIT'S PROFILE WITH RESPECT TO THE NUMBER OF ENGRAVING LOOPS.

Number of Engraving Loops	Measured Depth (μm)	Standard Deviation (μm)
30	768	66.56
32	817	68.68
34	849	79.09
36	929	76.75

For the sample, a carbon steel plate with a thickness of 2 mm was used. Artificial slits were engraved on the carbon steel plate using a laser engraver, where each artificial slit possessed the same width and height of 1 mm and 30 mm, respectively. Although the shape of the slit could be directly

created by using the laser engraver, a specific depth of the slit could not be directly obtained as it depended on the frequency, power, speed, and number of engraving loops of the laser. Therefore, only the number of engraving loops was varied at 30, 32, 34, and 36 to change the depth of the slits, while the frequency, power, and speed of the laser were fixed at 20 kHz, 70%, and 500 mm/s.

To allow a better interpretation of the measured magnetic flux leakage and eddy current signals, the assessment regarding the geometry and dimension of the fabricated artificial slits was required. Thus, the Olympus LEXT OLS5000 laser confocal microscope was used for this purpose. As illustrated in Fig. 3 (b), the surface of the slits was observed to be quite rough, which might be caused by the nonuniformity between each laser cut. From the 3D profile, the depth of the artificial slits was further calculated, where the actual depth of each slit was found to be approximately at 0.768, 0.817, 0.849, and 0.929 mm, as summarized in Table 2.

Using the engraved sample shown in Fig. 3 (a), a line scan measurement was performed from the back-side of the sample at a 1-mm interval. The MFL and eddy current signals were characterized, and their relationship due to the artificial slits was investigated with respect to the excitation frequency.

C. VECTOR CORRECTION

The conventional signal separation uses the current signal as the reference for the phase-sensitive detection technique. To implement a phase-sensitive detection technique that is insensitive to the variation of the magnetic property distribution, a dynamic referencing method using vector correction was applied after obtaining the results. Vector correction was performed by changing the reference signal during the separation of the real and imaginary components. This vector correction might further enhance the separation between the real and imaginary components, where the imaginary component could be further isolated with increased sensitivity to the changes in eddy current only. Thus, any correlation between the real component or flux leakage signal towards the imaginary component could be eliminated.

In the ideal situation, the intensity and phase of both S_1 and S_2 should be the same. However, in the presence of crack, and when one sensor is closer to the crack than the other, the eddy current distribution detected by that particular sensor would be higher compared to the other sensor. Therefore, it could be assumed that there are intensity and phase differences between the two sensors. In the proposed dynamic referencing method, the signals' references for both S_1 and S_2 were changed from the current source to the output of point 1 (left point), S_1, from the two points where the measurement was taken, as illustrated in Figs. 5 (a) and (b). The intensity and phase of vector-corrected $S_{1,RefS1}$ and $S_{2,RefS1}$ will vary depending on the magnetic response of S_1, unlike the static phase of the current source. Hence, in the case of a magnetic property distribution exists over a sample, the phase reference will be 'dynamic', depending on the location. The signal vectors S_1 and S_2 using the current signal as the reference can be expressed as,

$$S_1 = \sqrt{X_1^2 + Y_1^2}\cos\theta_1 + j\sqrt{X_1^2 + Y_1^2}\sin\theta_1, \quad (4)$$

$$S_2 = \sqrt{X_2^2 + Y_2^2}\cos\theta_2 + j\sqrt{X_2^2 + Y_2^2}\sin\theta_2. \quad (5)$$

The vector-corrected values using the current-referenced real X, and imaginary Y, components can be further expressed as,

$$S_{1,RefS1} = \sqrt{X_1^2 + Y_1^2}\cos(\theta_1 - \theta_1) + j\sqrt{X_1^2 + Y_1^2}\sin(\theta_1 - \theta_1), \quad (6)$$

$$S_{2,RefS1} = \sqrt{X_2^2 + Y_2^2}\cos(\theta_2 - \theta_1) + j\sqrt{X_2^2 + Y_2^2}\sin(\theta_2 - \theta_1). \quad (7)$$

Then, the differential signal $S_{1,RefS1}$-$S_{2,RefS1}$ = $Real_{RefS1}(S_1$-$S_2)$+j $Img._{RefS1}(S_1$-$S_2)$ can be used to reduce further the background noise detected by the sensors.

III. RESULTS AND DISCUSSIONS

A. SIMULATION OF FLUX LEAKAGE AND EDDY CURRENT SIGNALS

The results of both the real, $Real(B_{z,1}–B_{z,2})$ and imaginary, $Img.(B_{z,1}–B_{z,2})$ components of the differential magnetization signal, $B_{z,1}$-$B_{z,2}$ are shown in Fig. 6 (a) and (b), respectively. Here, $Real_{RefCurrent}(B_{z,1}–B_{z,2})$ and $Img._{RefCurrent}(B_{z,1}–B_{z,2})$ are the real and imaginary components of the intensity difference between S1 and S2 when the current source is used as the reference signal in the phase-sensitive detection. Meanwhile, $B_{z,1}$ and $B_{z,2}$ are the magnetic response in the sensitive axis of the AMR sensors (–*z*-direction) at the location of S1 and S2 in Fig. 1.

Figs. 6 (a) and (b) may also represent the real and imaginary components of the gradient magnetic field, which resulted due to the presence of two electromagnets (excitation coils). It could be seen that from the results, the overall value of the real part was higher compared to the imaginary part. Moreover, both real and imaginary values increased with frequency. This occurrence showed that real and imaginary parts could be represented by the flux leakage and eddy current signals, respectively. The penetration depth of the eddy current is hugely affected by the excitation frequency, where, within this simulation, the penetration depth at the lowest frequency (10 Hz) was approximately up to 4.83 mm, and the penetration depth at the highest frequency (510 Hz) was about 0.68 mm. Therefore, the flux leakage signal and eddy current signal were higher in the high-frequency region since the penetration depth is the

lowest, which causes both signals to accumulate nearer to the surface.

Besides that, as the frequency increased, the phase, as in Fig. 6 (c), was increased further (more lagging). This might also explain the increase in the imaginary component (eddy current signal) as the frequency was increased.

Moreover, within the FEM simulation, several FE models with the defective sample, as in Table 1, have been modeled and simulated. The FE models were varied with different positions of the excitation coils and their cores, namely from the position of −15 to 15 mm, thus mimicking a line scan measurement. The measurement resolution was 1 mm, giving a total of 31 measurement points. Fig. 7 illustrates the movement of the excitation coils along with their cores at the position of −15, 0, and 15 mm.

From Fig. 7, the surface plot of the simulation results represents the real, $Real_{RefCurrent}(B_z)$ and imaginary, $Img._{RefCurrent}(B_z)$ components using the current signal as the reference, while the line contour plot represents the magnetic vector potential. The simulation was conducted at nine different frequencies, within 10-510 Hz, while the thickness of the sample was also varied at 2, 4, 6, 8, and 10 mm. Meanwhile, the slit was modeled on the back-side of the sample with depth and width set to 1 mm.

Afterward, the results of the phase-corrected signals are plotted in Fig. 8. The $Real_{RefBz,1}(B_{z,1}–B_{z,2})$ and $Img._{RefBz,1}(B_{z,1}–B_{z,2})$ are the real and imaginary components of the intensity difference between S1 and S2 when S1 ($B_{z,1}$) is used as the reference signal in the phase-sensitive detection. From Fig. 8 (a), it was evident that the real component referenced to $B_{z,1}$, $Real_{RefBz,1}(B_{z,1}–B_{z,2})$ was similar to $Real_{RefCurrent}(B_{z,1}–B_{z,2})$ in Fig. 6 (a), where their magnitudes were almost the same. However, from Fig. 8 (b), the pattern of the imaginary component referenced to $B_{z,1}$, $Img._{RefBz,1}(B_{z,1}–B_{z,2})$ could be seen to be modified from $Img._{RefCurrent}(B_{z,1}–B_{z,2})$ of Fig. 6 (b), where the imaginary component became approximately 0 T regardless of frequency. This showed that the imaginary component had been isolated from the real component. However, in the case of the 2-mm plate at high frequency, the slight deviation might be affected by the strong eddy current signals near the surface. Meanwhile, a constant phase change of 0° was observed across the measurement spectrum.

The results of the line scan measurements for the real, $Real_{RefBz,1}(B_{z,1} - B_{z,2})$ and imaginary parts, $Img._{RefBz,1}(B_{z,1} - B_{z,2})$ using $B_{z,1}$ as the reference, are shown in Figs. 9 and 10, respectively. Here, the 510-Hz waveforms for every sample thickness were used as the baseline signal relative to other frequency waveforms. From Fig. 9, the location of the slit could be represented by the minimum and maximum values of the real part of the differential magnetic response, *i.e.*, $B_{z,1}–B_{z,2}$. Although, as the frequency increased, the overall signal tended to be decreased, and its pattern started to change at frequency 410-510 Hz for the 2-mm sample and frequency 70-110 Hz for the 4-mm sample. At a low-frequency region, the penetration depth was expected to be high hence allowing the excitation magnetic flux to penetrate deeper within the sample. In this case, the flux leakage could occur at the slit on the back-side of the sample due to the higher penetration depth, causing the magnetization signal of the sample measured at the front surface to be minimum at the location of the back-side slit. The increase of the excitation frequency would reduce the penetration depth, hence, concentrating the flux distribution at the front surface. This would result in the magnetic flux leakage on the front surface at the slit location, producing a maximum in the real component $Real_{RefBz,1}(B_{z,1} - B_{z,2})$, as shown in Fig. 9. Furthermore, as the thickness increased, the pattern started to diminish due to low penetration depth, and the real part of the signals could not penetrate deeper to reach the back-side slit.

Meanwhile, the pattern was different for the imaginary part of the differential magnetic response. The signal that represented the location of the slit was defined to be at the middle between the transition from the maximum value to the minimum value. Nonetheless, the pattern started to diminish as the frequency and sample thickness were increased, as in Fig. 10. Eventually, the imaginary signal no longer detected changes in the eddy current and would only show the gradient field of the eddy current, and the same was true with its real counterpart. This was most likely due to the low penetration depth, where the higher the frequency, the lower the penetration depth.

Then, from the raw waveform, the delta values of the real, $\Delta(Real_{RefBz,1}(B_{z,1}–B_{z,2}))$ and imaginary components, $\Delta(Img._{RefBz,1}(B_{z,1}–B_{z,2}))$ were calculated for every line scan measurement by calculating the difference between the peak and trough as in Fig. 11 (a) for the real part, $\Delta(Real_{RefBz,1}(B_{z,1}–B_{z,2}))$ and Fig. 11 (b), for the imaginary part, $\Delta(Img._{RefBz,1}(B_{z,1}–B_{z,2}))$. The results for every frequency were plotted versus sample thickness, as illustrated in Fig. 12.

For the real part, it could be concluded that $\Delta(Real_{RefBz,1}(B_{z,1}–B_{z,2}))$ decreased with increasing thickness and frequency. A similar trend was observed for the imaginary part. However, the case was different with increasing frequency. From Fig. 12 (b), it could be seen that $\Delta(Img._{RefBz,1}(B_{z,1} - B_{z,2}))$ peaked at a certain frequency region for every sample thickness. For the 2-mm sample, the $\Delta(Img._{RefBz,1}(B_{z,1} - B_{z,2}))$ peaked around the region of 90-160 Hz. A left shift of the peaks in the $\Delta(Img._{RefBz,1}(B_{z,1} - B_{z,2}))$ curve was also observed with increasing sample thickness.

B. EXPERIMENTAL RESULTS

An experimental study on the dependency of both flux leakage and eddy current signals as a function of excitation frequency was conducted. The range of excitation frequencies that were to be analyzed was set from 10 to 510 Hz. Meanwhile, the excitation amplitude and lift-off were fixed at 0.3 A and 0.81 mm. The results for the raw waveform of the flux leakage, $Real_{RefS1}(S_1−S_2)$ and eddy current signals, $Img._{RefS1}(S_1−S_2)$ are shown in Figs. 13 and 14,

respectively. The signals obtained for the experiments were the differential signal of the outputs of sensor 1, S_1, and sensor 2, S_2, using sensor 1 as the reference, *i.e.*, $Real_{RefS1}(S_1-S_2)$ for the real component and $Img._{RefS1}(S_1-S_2)$ for the imaginary component. The output signals of S_1 and S_2 were the B_z components and amplified with a gain of 129.

It was found that the patterns of the measured waveforms agreed with the simulation results. For the real part, the location of the slit was defined to be the minimum voltage value, while for the imaginary part, it was in the middle of the transition from the maximum to the minimum values. In Figs. 9 and 13, it could be observed that the signal baselines of the waveforms were reduced as the frequency was increased, inferring the magnetization signal from the sample was reduced due to the reduction in the penetration depth. However, slight differences in the sensors' alignment, such as lift-off, had caused the signal baselines in Fig. 14 to show a negative offset and not centered to 0 V at the slit location compared to the simulated imaginary component shown in Fig. 10. Further signal processing to remove the signal baselines could be performed to obtain a zero-crossing point corresponding to the defect location.

Furthermore, the signal characteristics shown in the real and imaginary components of the differential signals were close to the signal characteristics found in the ACFM method for the B_x and B_z components, respectively. It is worth noting that the typical ACFM technique utilizes horizontally oriented solenoid coils with respect to the inspection surface to induce a uniform eddy current in a relatively large area compared to other eddy current measurement techniques [27]. A similar eddy current signal characteristic could be expected in the ACFM and ECT techniques since these eddy current measurement techniques evaluate the disturbance of eddy current due to defects. However, the ACFM technique is sensitive to the eddy current direction, reflected in the B_x and B_z components. On the other hand, the developed probe separated the magnetic flux leakage and eddy current signals based on their phase information.

Consequently, by using the same method as the calculation of $\Delta(Real_{RefBz,1}(B_{z,1}-B_{z,2}))$ and $\Delta(Img._{RefBz,1}(B_{z,1}-B_{z,2}))$ in the simulation (Figs. 11 (a) and (b)), the delta values of the real, $\Delta(Real_{RefS1}(S_1-S_2))$ and imaginary components, $\Delta(Img._{RefS1}(S_1-S_2))$ from the measured signals were calculated from the raw waveforms and plotted as a function of slit depth as in Fig. 15. It could be observed that both $\Delta(Real_{RefS1}(S_1-S_2))$ and $\Delta(Img._{RefS1}(S_1-S_2))$ increased with increasing slit depth. Additionally, the excitation frequency also affected the overall delta values of the flux leakage, $\Delta(Real_{RefS1}(S_1-S_2))$ and eddy current signals, $\Delta(Img._{RefS1}(S_1-S_2))$. For the magnetic flux leakage signal, the overall $\Delta(Real_{RefS1}(S_1-S_2))$ seemed to be decreased with the increase of frequency. Meanwhile, the overall eddy current signal $\Delta(Img._{RefS1}(S_1-S_2))$ increased along with the frequency and peaked at 160 Hz before decreasing.

Then, the gradient of trendlines of delta values of $\Delta(Real_{RefS1}(S_1-S_2))$ and $\Delta(Img._{RefS1}(S_1-S_2))$ at every frequency was calculated and plotted as shown in Fig. 16. From the plot, the gradient of trendlines of the flux leakage signal $\Delta(Real_{RefS1}(S_1-S_2))$ could be said to be decreased with increasing frequency. However, the gradient of trendlines of the eddy current signal $\Delta(Img._{RefS1}(S_1-S_2))$ increased with respect to frequency until it culminated at around 160 Hz. Additionally, the magnitude of both real and imaginary trendlines $((\Delta(Real_{RefS1}(S_1-S_2)))^2 + (\Delta(Img._{RefS1}(S_1-S_2)))^2)^{1/2}$ showed that the optimum frequency range for both flux leakage and eddy current signals was between 110-210 Hz. Therefore, it could be inferred that defect detection using both flux leakage and eddy current signals would be significantly benefited within this frequency region.

C. COMPARISON BETWEEN SIMULATION AND EXPERIMENTAL RESULTS BY USING LISSAJOUS CURVE

Further analysis involving both the simulation and experimental results was done by comparing their Lissajous curves. Although simulations using a 3D model would result in a more accurate comparison to the experimental results, it could be expected that the simulation based on the 2D cross-sectional model would be sufficient for validating the agreement between the simulation and experimental results. As the Lissajous curve is represented by the plot of real versus imaginary values, the raw waveforms of both real and imaginary components from the line scan measurements were used.

The penetration depth of the eddy current for the frequency range from 10 to 510 Hz varied from 4.83 to 0.68 mm for the sample used in this study. Therefore, a sample thickness within this penetration depth was selected, where the simulation results of the 2-mm thick sample with a slit depth of 1 mm, and the experimental results of the 2-mm carbon steel plate with a slit depth of 0.929 mm, were compared.

Fig. 17 shows the Lissajous curves for the simulation and experimental results at the frequency of 30 (low-frequency region), 160 (optimum frequency region) and 410 Hz (high-frequency region). Here, the vertical and horizontal axes for the experimental results were normalized for a better comparison to the simulation results. As discussed in the previous section, the location of the slits could be identified from the minimum value of the real part for the frequency range of less than 210 Hz (see Fig. 13). However, the pattern started changing as the frequency was increased beyond 210 Hz, where the location of the slits could be identified from the maximum value of the real component. As evident from both the simulation and experimental plots, the split in the Lissajous curves at the location of the slit showed a V-shape characteristic. The inner angle of the V-shape curve became wider as the frequency was increased (from 30 Hz to 160

Hz). Then, at 410 Hz, a complete transformation of the V-shape curve's pointing direction was observed.

From the similarities between the simulation and experimental results, it could be concluded that a reasonably good agreement was found between them. The slight differences between the simulation and experimental results were caused by the 2D model used in the simulation. Furthermore, although the nonlinear magnetization property of the carbon steel sample has already been taken into account in the simulation, slight differences in the magnetic properties of the sample in the simulation and the actual sample could not be excluded. Nonetheless, the simulation and experimental results proved that the Lissajous curve characteristic could be utilized to enable defect detection using magnetic flux leakage and eddy current signals.

IV. CONCLUSION

In this study, both MFL and EC techniques were used in the evaluation of back-side slits, where each signal was separated by using the phase-sensitive detection technique. An FE model was used to verify both flux leakage and eddy current signals, where it strongly suggested that the separation of both flux leakage and eddy current signals were achievable, and their characteristics could be utilized to improve defect detection.

Furthermore, by applying the dynamic referencing technique, the resulted imaginary component could be utilized to sensitively sense the change of eddy current with a negligible contribution of the magnetic flux leakage signal represented by the real component. Furthermore, the simulation using a back-side slit showed that the pattern of real and imaginary components could be used to estimate the sample thickness and the slit location.

Finally, by using the same probe configuration as in the simulation, a differential AMR magnetic probe was fabricated to verify the simulation results. A 2-mm carbon steel plate with back-side artificial slits of varying depths was used as the sample. The patterns of the raw waveforms resulted from artificial slits on the 2-mm carbon steel plate, agreed with the simulated real and imaginary components. The results showed that the slit depth could be estimated by varying the excitation frequency, where the optimum frequency region was found to be in the region from 110 to 210 Hz.

Although the current study used a carbon steel sample with the specified dimensions, it is expected that the proposed method can be applied for other ferrous metals with different dimensions. In the future, we will expand our study to elucidate the effects of material types and dimensions on the proposed method. Furthermore, for future recommendations, the configuration of the magnetic probe can be further modified to improve the detection sensitivity of both flux leakage and the eddy current signals. Besides that, since the separation of the magnetic flux leakage and eddy current signals has been proved to be achievable, further integration between the MFL and EC techniques during defect evaluations can be expected. The integration of both techniques will increase the potential and performance of an NDT probe for better detection of either back-side or subsurface defects.

ACKNOWLEDGMENT

The authors would like to thank the Ministry of Higher Education for providing financial support under Fundamental Research Grant Scheme (FRGS) No. FRGS/1/2019/TK04/UMP/02/4 (University reference RDU1901154) and Universiti Malaysia Pahang for laboratory facilities as well as additional financial support under Internal Research grant RDU1903100. A special thank you to Dr. Aiman Mohd Halil on behalf of the Faculty of Mechanical and Automotive Engineering Technology, Universiti Malaysia Pahang, for his contributions toward this research.

REFERENCES

[1] A. McCrea, D. Chamberlain, and R. Navon, "Automated inspection and restoration of steel bridges—a critical review of methods and enabling technologies," *Autom. Constr.*, vol. 11, no. 4, pp. 351–373, Jun. 2002, doi: 10.1016/S0926-5805(01)00079-6.

[2] M. I. . Ahmad, A. Arifin, and S. Abdullah, "Evaluation of magnetic flux leakage signals on fatigue crack growth of mild steel," *J. Mech. Eng. Sci.*, vol. 9, no. January, pp. 1727–1733, Dec. 2015, doi: 10.15282/jmes.9.2015.18.0166.

[3] R. Ghoni, M. Dollah, A. Sulaiman, and F. M. Ibrahim, "Defect Characterization Based on Eddy Current Technique: Technical Review," *Adv. Mech. Eng.*, vol. 6, p. 182496, Jan. 2014, doi: 10.1155/2014/182496.

[4] H. Chu and Z. Wang, "A vision-based system for post-welding quality measurement and defect detection," *Int. J. Adv. Manuf. Technol.*, vol. 86, no. 9–12, pp. 3007–3014, Oct. 2016, doi: 10.1007/s00170-015-8334-1.

[5] B. M. Abdullah, A. Mason, and A. Al-Shamma'a, "Defect detection of the weld bead based on electromagnetic sensing," *J. Phys. Conf. Ser.*, vol. 450, p. 012039, Jun. 2013, doi: 10.1088/1742-6596/450/1/012039.

[6] G.-R. Tillack, C. Nockemann, and C. Bellon, "X-ray modeling for industrial applications," *NDT E Int.*, vol. 33, no. 7, pp. 481–488, Oct. 2000, doi: 10.1016/S0963-8695(00)00019-0.

[7] Ngon Dang Thien, Cuong Le Chi, and Ha Nguyen Ngoc, "An approach to the automatic detection of weld defects in radiography films using digital image processing," in *2017 International Conference on System Science and Engineering (ICSSE)*, Jul. 2017, pp. 371–374, doi: 10.1109/ICSSE.2017.8030899.

[8] L. Goglio and M. Rossetto, "Ultrasonic testing of adhesive bonds of thin metal sheets," *NDT E Int.*, vol. 32, no. 6, pp. 323–331, 1999, doi: 10.1016/S0963-8695(98)00076-0.

[9] J. Jiao, J. Sun, N. Li, G. Song, B. Wu, and C. He, "Micro-crack detection using a collinear wave mixing technique," *NDT E Int.*, vol. 62, pp. 122–129, 2014, doi: 10.1016/j.ndteint.2013.12.004.

[10] A. Jander, C. Smith, and R. Schneider, "Magneto-resistive sensors for non-destructive evaluation (Invited Paper)," in *Advanced Sensor Technologies for Nondestructive Evaluation and Structural Health Monitoring*, May 2005, vol. 5770, p. 1, doi: 10.1117/12.601826.

[11] J. Y. Lee, S. J. Lee, D. C. Jiles, M. Garton, R. Lopez, and L. Brasche, "Sensitivity analysis of simulations for magnetic particle inspection using the finite-element method," *IEEE Trans. Magn.*, vol. 39, no. 6, pp. 3604–3606, Nov. 2003, doi: 10.1109/TMAG.2003.816152.

[12] T. Sasayama, T. Ishida, M. Matsuo, and K. Enpuku, "Thickness Measurement of an Iron Plate Using Low-Frequency Eddy Current Testing With an HTS Coil," *IEEE Trans. Appl. Supercond.*, vol. 26, no. 5, pp. 1–5, Aug. 2016, doi: 10.1109/TASC.2016.2535366.

[13] N. Kasai, Y. Fujiwara, K. Sekine, and T. Sakamoto, "Evaluation of back-side flaws of the bottom plates of an oil-storage tank by the RFECT," *NDT E Int.*, vol. 41, no. 7, pp. 525–529, Oct. 2008, doi: 10.1016/j.ndteint.2008.05.002.

[14] J. García-Martín, J. Gómez-Gil, and E. Vázquez-Sánchez, "Non-Destructive Techniques Based on Eddy Current Testing," *Sensors*, vol. 11, no. 3, pp. 2525–2565, Feb. 2011, doi: 10.3390/s110302525.

[15] M. M. Saari, T. Kiwa, and K. Tsukada, "Design of Eddy Current Testing Probe for Surface Defect Evaluation," *Int. J. Automot. Mech. Eng.*, vol. 16, no. 1, pp. 6357–6367, 2019, doi: 10.15282/ijame.16.1.2019.19.0481.

[16] K. Tsukada, M. Yoshioka, Y. Kawasaki, and T. Kiwa, "Detection of back-side pit on a ferrous plate by magnetic flux leakage method with analyzing magnetic field vector," *NDT E Int.*, vol. 43, no. 4, pp. 323–328, Jun. 2010, doi: 10.1016/j.ndteint.2010.01.004.

[17] M. A. H. P. Zaini, M. M. Saari, N. A. Nadzri, A. M. Halil, A. J. S. Hanifah, and M. Ishak, "Effect of Excitation Frequency on Magnetic Response Induced by Front- and Back-Side Slits Measured by a Differential AMR Sensor Probe," in *Lecture Notes in Electrical Engineering*, vol. 632, no. July, 2020, pp. 15–24.

[18] M. J. Sablik and B. Augustyniak, "Magnetic Methods of Non-destructive Evaluation," in *Wiley Encyclopedia of Electrical and Electronics Engineering*, no. 23, Hoboken, NJ, USA: John Wiley & Sons, Inc., 1999, pp. 12–31.

[19] D. C. Jiles, "Review of magnetic methods for non-destructive evaluation (Part 2)," *NDT Int.*, vol. 23, no. 2, pp. 83–92, Apr. 1990, doi: 10.1016/0308-9126(90)91892-W.

[20] M. A. H. P. Zaini, M. M. Saari, N. A. Nadzri, A. Mohd Halil, and K. Tsukada, "An MFL Probe using Shiftable Magnetization Angle for Front and Back Side Crack Evaluation," in *2019 IEEE 15th International Colloquium on Signal Processing & Its Applications (CSPA)*, Mar. 2019, no. March, pp. 157–161, doi: 10.1109/CSPA.2019.8696064.

[21] W. S. Singh, B. P. C. Rao, S. Vaidyanathan, T. Jayakumar, and B. Raj, "Detection of leakage magnetic flux from near-side and far-side defects in carbon steel plates using a giant magneto-resistive sensor," *Meas. Sci. Technol.*, vol. 19, no. 1, 2008, doi: 10.1088/0957-0233/19/1/015702.

[22] F. I. Al-Naemi, J. P. Hall, and A. J. Moses, "FEM modelling techniques of magnetic flux leakage-type NDT for ferromagnetic plate inspections," *J. Magn. Magn. Mater.*, 2006, doi: 10.1016/j.jmmm.2006.02.225.

[23] J. Atzlesberger, B. G. Zagar, R. Cihal, M. Brummayer, and P. Reisinger, "Sub-surface defect detection in a steel sheet," *Meas. Sci. Technol.*, vol. 24, no. 8, 2013, doi: 10.1088/0957-0233/24/8/084003.

[24] N. A. Nadzri, M. M. Saari, M. A. H. P. Zaini, A. M. Halil, A. J. S. Hanifah, and M. Ishak, "Depth Evaluation of Slits on Galvanized Steel Plate Using a Low Frequency Eddy Current Probe," in *Proceedings of the 5th International Conference on Electrical, Control & Computer Engineering (InECCE2019)*, 2020, pp. 59–66.

[25] K. Tsukada, M. Hayashi, Y. Nakamura, K. Sakai, and T. Kiwa, "Small Eddy Current Testing Sensor Probe Using a Tunneling Magnetoresistance Sensor to Detect Cracks in Steel Structures," *IEEE Trans. Magn.*, vol. PP, pp. 1–5, 2018, doi: 10.1109/TMAG.2018.2845864.

[26] B. Lebrun, Y. Jayet, and J.-C. Baboux, "Pulsed eddy current signal analysis: application to the experimental detection and characterization of deep flaws in highly conductive materials," *NDT E Int.*, vol. 30, no. 3, pp. 163–170, Jun. 1997, doi: 10.1016/S0963-8695(96)00072-2.

[27] M. P. Papaelias, M. C. Lugg, C. Roberts, and C. L. Davis, "High-speed inspection of rails using ACFM techniques," *NDT E Int.*, vol. 42, no. 4, pp. 328–335, 2009, doi: 10.1016/j.ndteint.2008.12.008.

[28] W. Cheng, "Pulsed Eddy Current Testing of Carbon Steel Pipes' Wall-thinning Through Insulation and Cladding," *J. Nondestruct. Eval.*, vol. 31, no. 3, pp. 215–224, Sep. 2012, doi: 10.1007/s10921-012-0137-9.

[29] F. Vacher, J. M. Decitre, C. Fermon, and M. Pannetier, "Non Destructive Testing with GMR Magnetic Sensor Arrays," *9th Eur. Conf. NDT - Sept. 2006 - Berlin (ECNDT 2006)*, no. 2006–11, pp. 1–8, 2006, [Online]. Available: https://www.ndt.net/article/ecndt2006/doc/Tu.4.4.2.pdf.

[30] D. Wu, Z. Liu, X. Wang, and L. Su, "Composite magnetic flux leakage detection method for pipelines using alternating magnetic field excitation," *NDT E Int.*, vol. 91, no. July, pp. 148–155, 2017, doi: 10.1016/j.ndteint.2017.07.002.

[31] G. Yang *et al.*, "Pulsed eddy-current based giant magneto-resistive system for the inspection of aircraft structures," *IEEE Trans. Magn.*, vol. 46, no. 3 PART 2, pp. 910–917, 2010, doi: 10.1109/TMAG.2009.2032330.

[32] M. A. H. P. Zaini, M. M. Saari, N. A. Nadzri, A. M. Halil, A. J. S. Hanifah, and K. Tsukada, "Evaluation of Back-Side Slits with Sub-millimeter Resolution Using a Differential AMR Probe," in *Proceedings of the 11th National Technical Seminar on Unmanned System Technology 2019*, 2021, pp. 319–328.

This article has been accepted for publication in a future issue of this journal, but has not been fully edited. Content may change prior to final publication. Citation information: DOI 10.1109/ACCESS.2021.3123421, IEEE Access

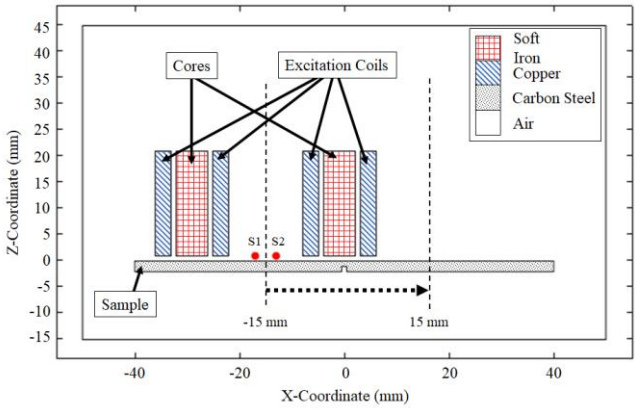

Figure 1 **The 2-D FE model as sketched in a FEM software.**

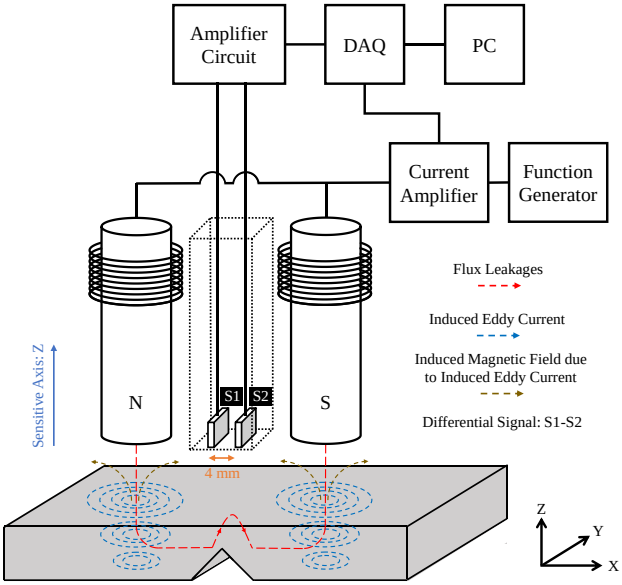

Figure 2 **Probe arrangement and its connection to the measurement system with 4 mm distance between the two AMR sensors. The sensor sensitivity is in – *z*-direction. The differential signal is also obtained by S1–S2.**

This article has been accepted for publication in a future issue of this journal, but has not been fully edited. Content may change prior to final publication. Citation information: DOI 10.1109/ACCESS.2021.3123421, IEEE Access

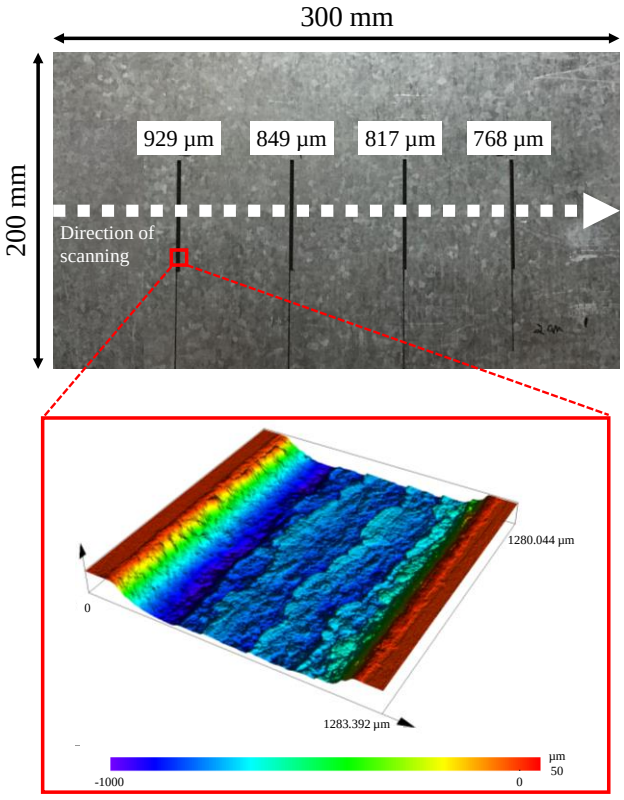

Figure 3 **The artificial slits created on the sample with different depths. and the 3-D profile of the engraved artificial slits with depth of 929 µm obtained from the Olympus LEXT OLS5000 laser confocal microscope.**

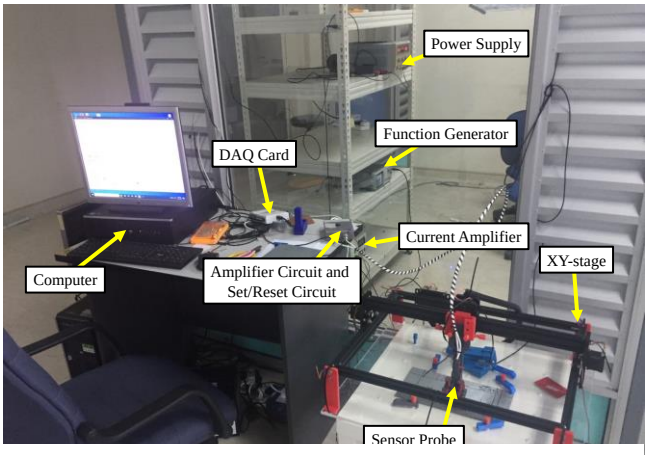

Figure 4 **Photograph of the complete measurement system**

This article has been accepted for publication in a future issue of this journal, but has not been fully edited. Content may change prior to final publication. Citation information: DOI 10.1109/ACCESS.2021.3123421, IEEE Access

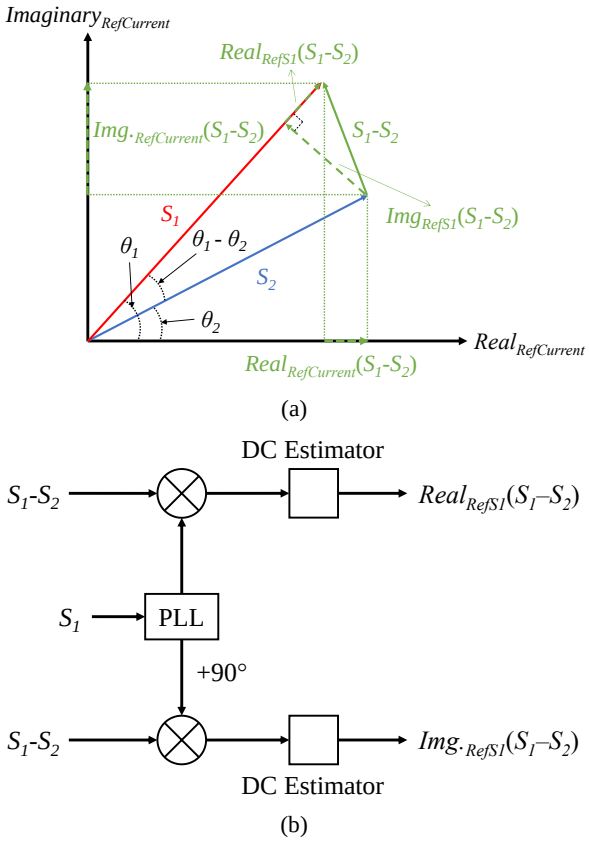

Figure 5 **(a) Phasor diagram of S_1, S_2 and their differential component for static and dynamic referencing method. In the dynamic referencing method, the phase reference of S_1 will vary depending on the output of S_1, unlike the static phase reference using the current source. (b) Block diagram of phase-sensitive detection implemented in LabVIEW.**

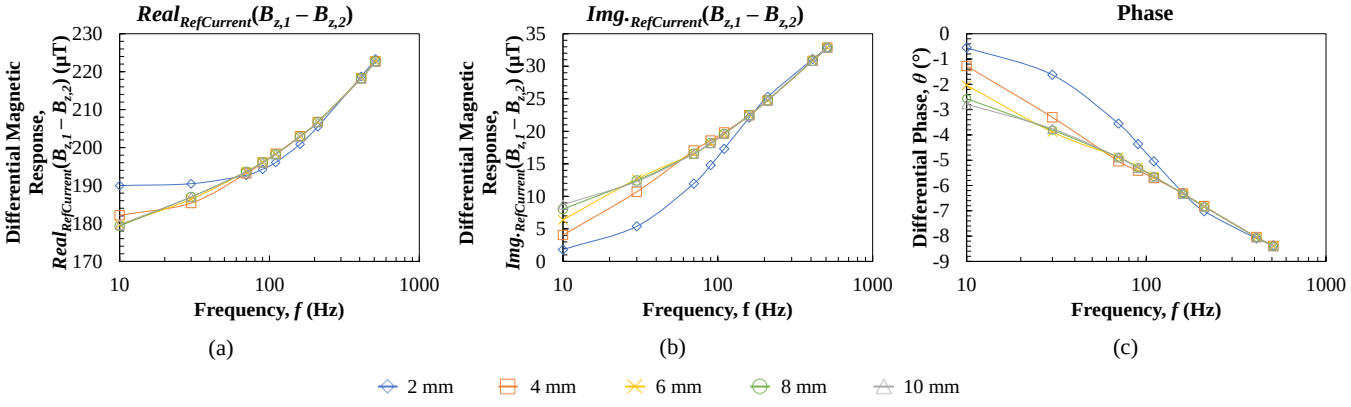

Figure 6 **(a) The real and (b) imaginary part of the magnetic response as well as (c) the phase obtained from the simulation conducted on the defectless sample using the current signal as the reference.**

This article has been accepted for publication in a future issue of this journal, but has not been fully edited. Content may change prior to final publication. Citation information: DOI 10.1109/ACCESS.2021.3123421, IEEE Access

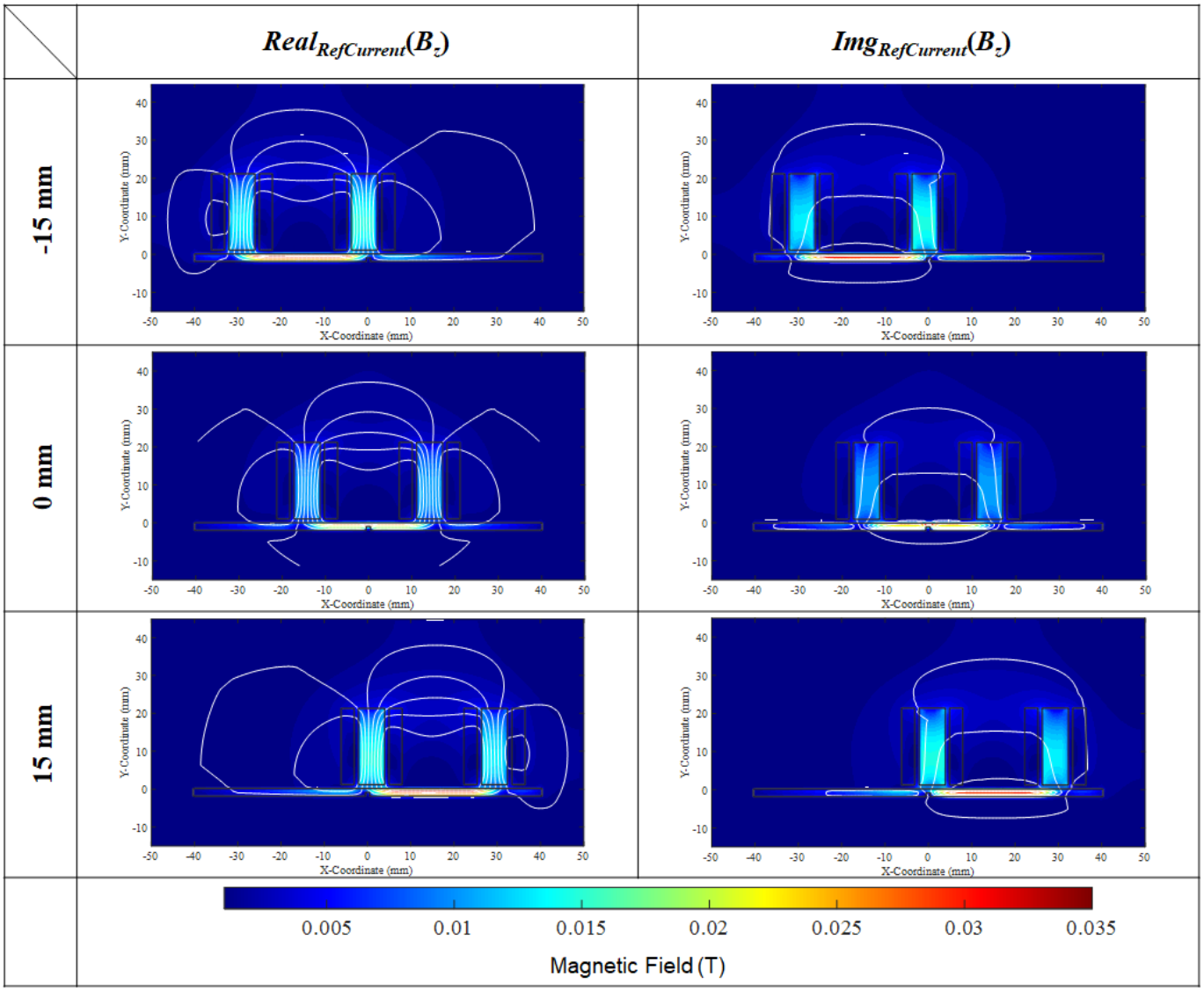

Figure 7 The simulation results of the real part and imaginary components at the position of –15, 0, and 15 mm.

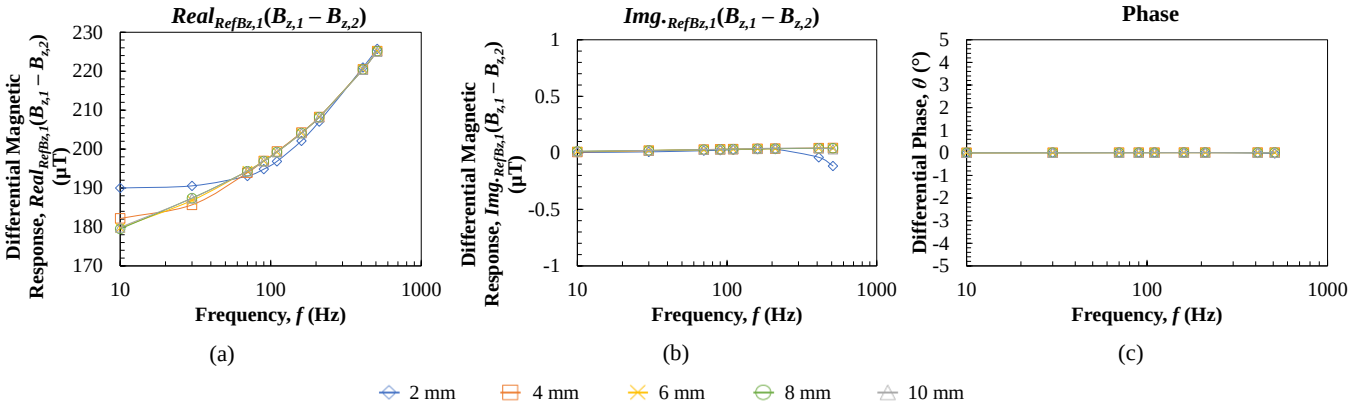

Figure 8 (a) The real and (b) imaginary part of the magnetic response as well as (c) the phase obtained from the simulation conducted on the defectless sample using S_1 ($B_{z,1}$) as the reference signal.

This article has been accepted for publication in a future issue of this journal, but has not been fully edited. Content may change prior to final publication. Citation information: DOI 10.1109/ACCESS.2021.3123421, IEEE Access

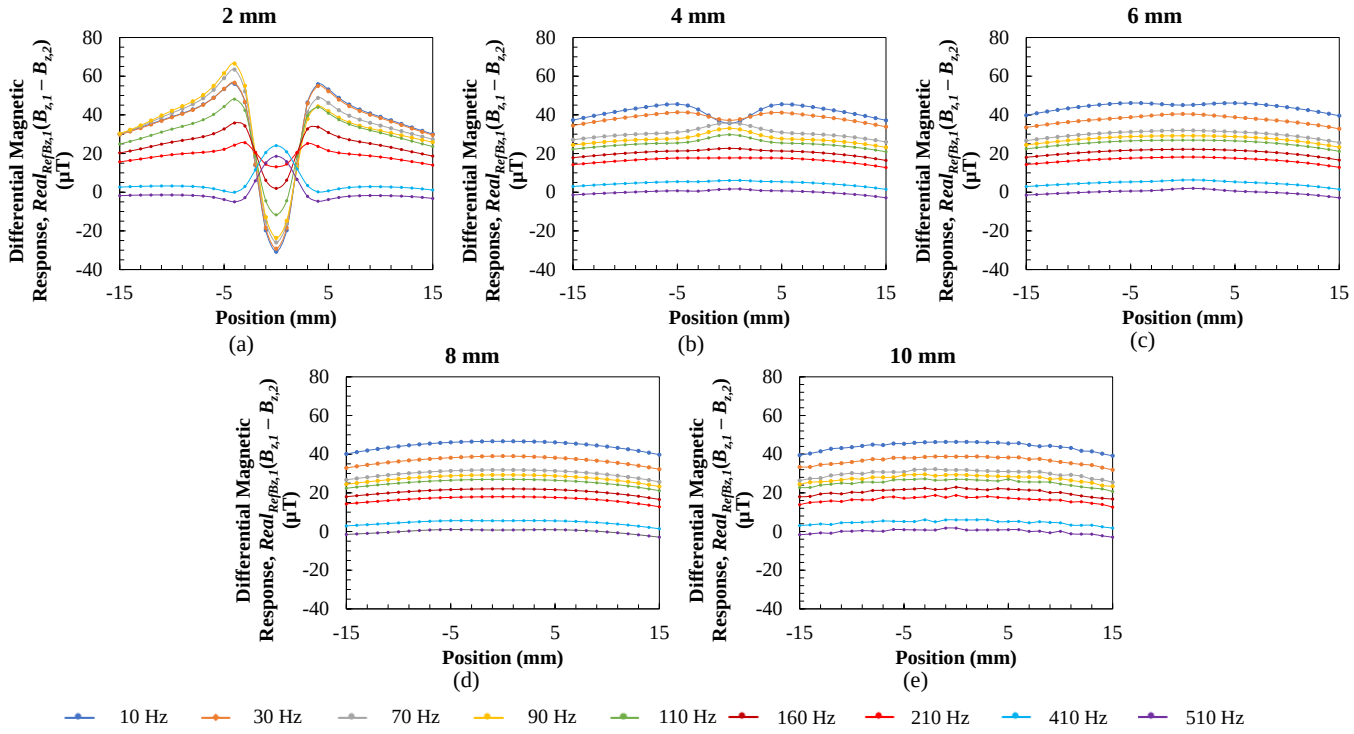

Figure 9 The waveforms of the simulated real components obtained from the line scan measurement at various frequencies ranging from 10 to 510 Hz for samples with a thickness of (a) 2 mm, (b) 4 mm, (c) 6 mm, (d) 8 mm and (e) 10 mm. Every sample had a back-side slit with a width and depth of 1 mm. The 510-Hz waveforms for every sample thickness were used as the baseline signal relative to other frequency waveforms.

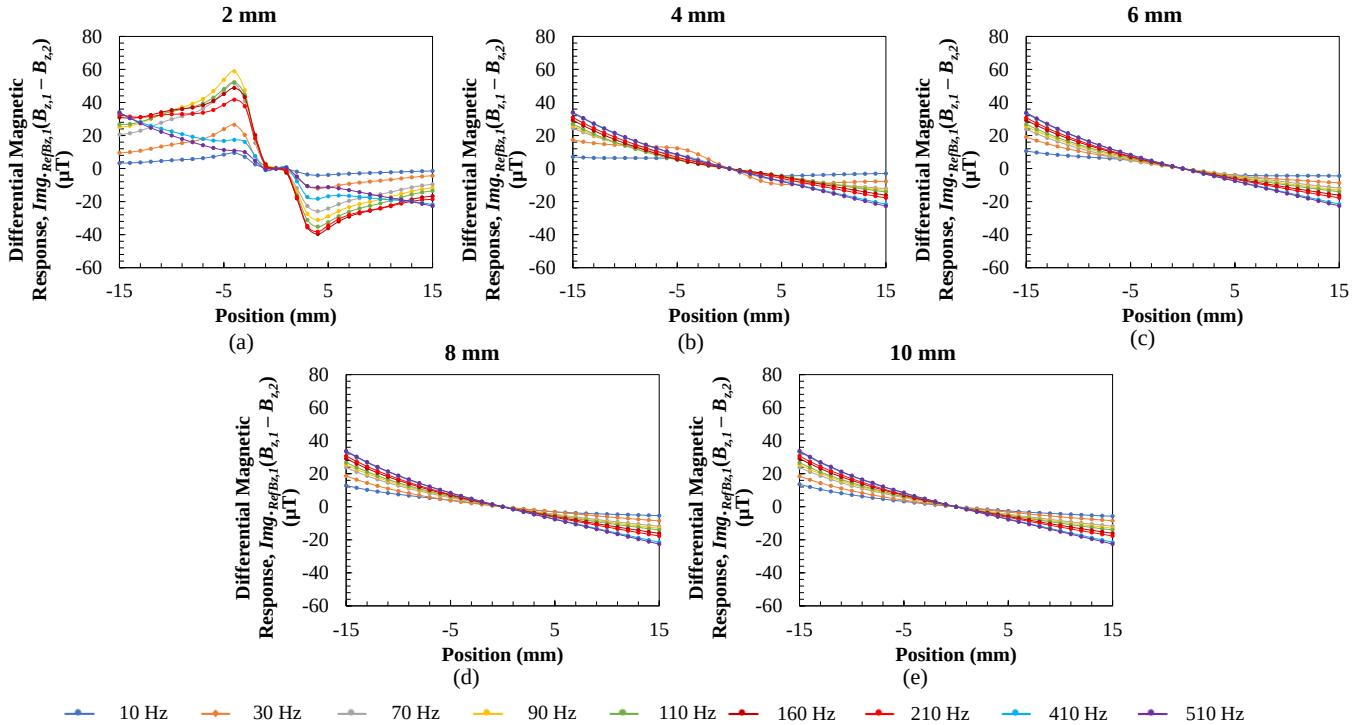

Figure 10 The waveforms of the simulated imaginary components obtained from the line scan measurement at various frequencies ranging from 10 to 510 Hz for samples with a thickness of (a) 2 mm, (b) 4 mm, (c) 6 mm, (d) 8 mm and (e) 10 mm. Every sample had a back-side slit with a width and depth of 1 mm.

This article has been accepted for publication in a future issue of this journal, but has not been fully edited. Content may change prior to final publication. Citation information: DOI 10.1109/ACCESS.2021.3123421, IEEE Access

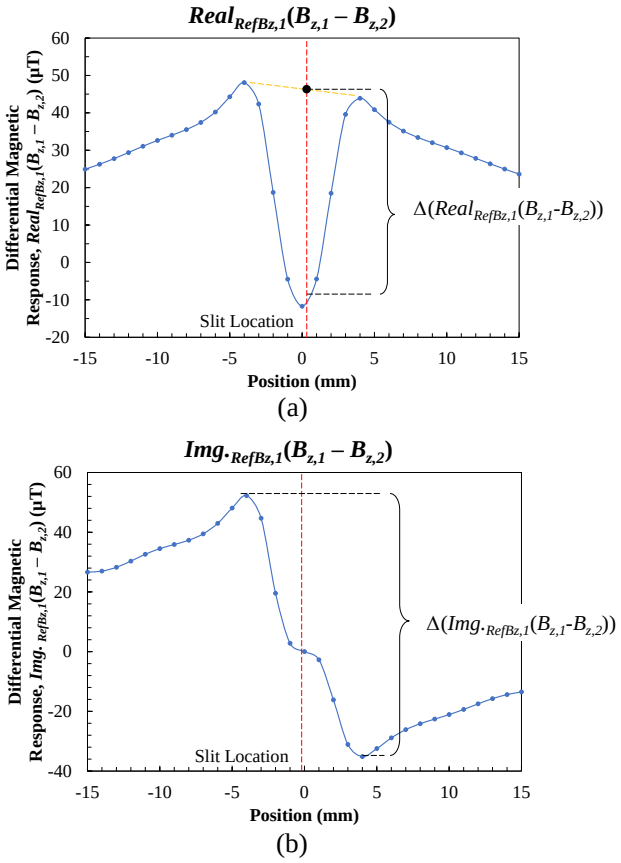

Figure 11 The waveforms of (a) real and (b) imaginary components referenced to S_1 ($B_{z,1}$) at the frequency of 110 Hz for the 2-mm sample. The waveform of the real components in (a) was plotted relative with the baseline signal of the 510-Hz waveform.

This article has been accepted for publication in a future issue of this journal, but has not been fully edited. Content may change prior to final publication. Citation information: DOI 10.1109/ACCESS.2021.3123421, IEEE Access

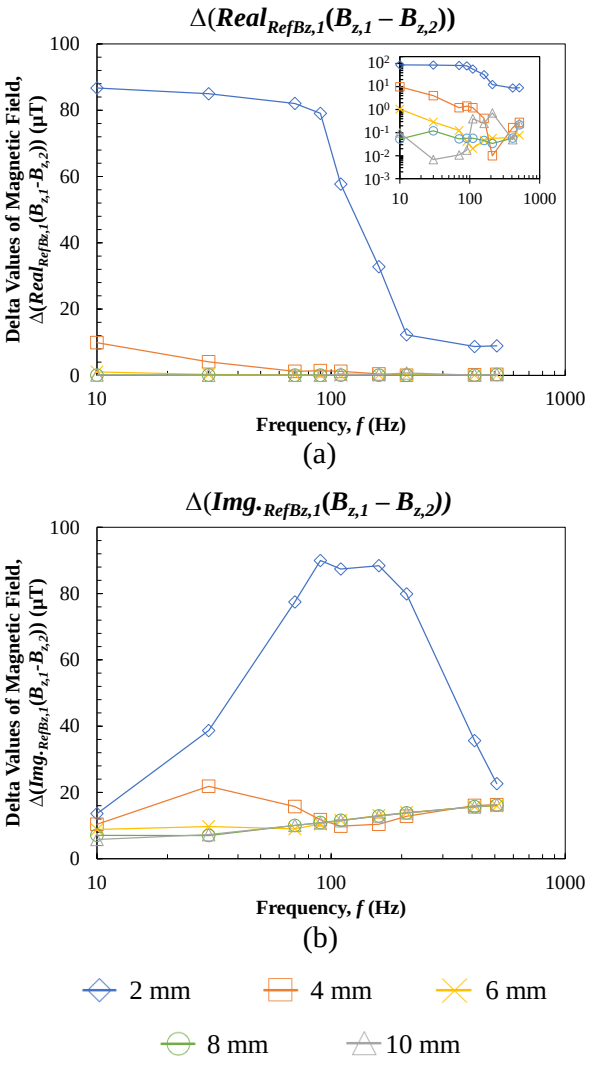

Figure 12 The delta values of the magnetic field for (a) real and (b) imaginary components versus frequency for the sample thickness of 2, 4, 6, 8, and 10 mm.

This article has been accepted for publication in a future issue of this journal, but has not been fully edited. Content may change prior to final publication. Citation information: DOI 10.1109/ACCESS.2021.3123421, IEEE Access

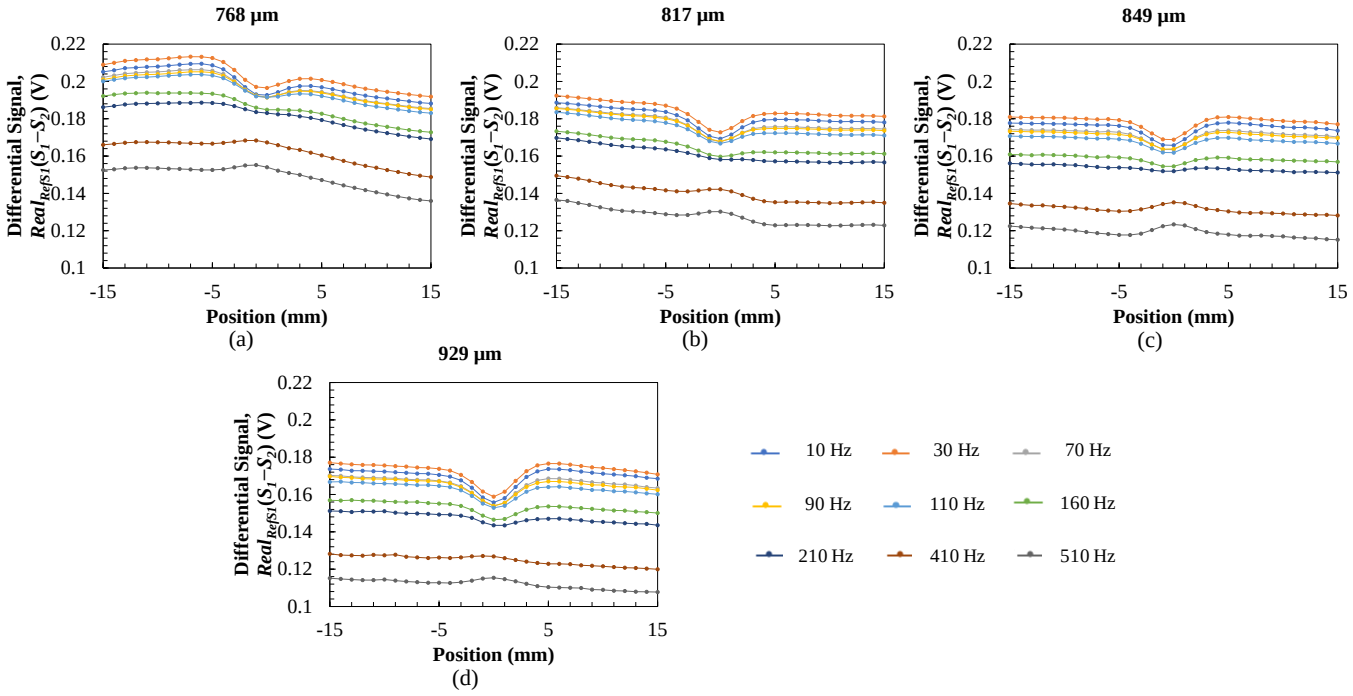

Figure 13 The waveforms of the measured real components obtained from the differential signals of sensor 1 and sensor 2 using sensor 1 as the reference, $S_{1,RefS1}$–$S_{2,RefS1}$ at (a) 0.768-mm, (b) 0.817-mm (c) 0.849-mm and (d) 0.929-mm slits. The frequency was varied from 10 to 510 Hz and the sensor outputs were the B_z components and amplified by a gain of 129.

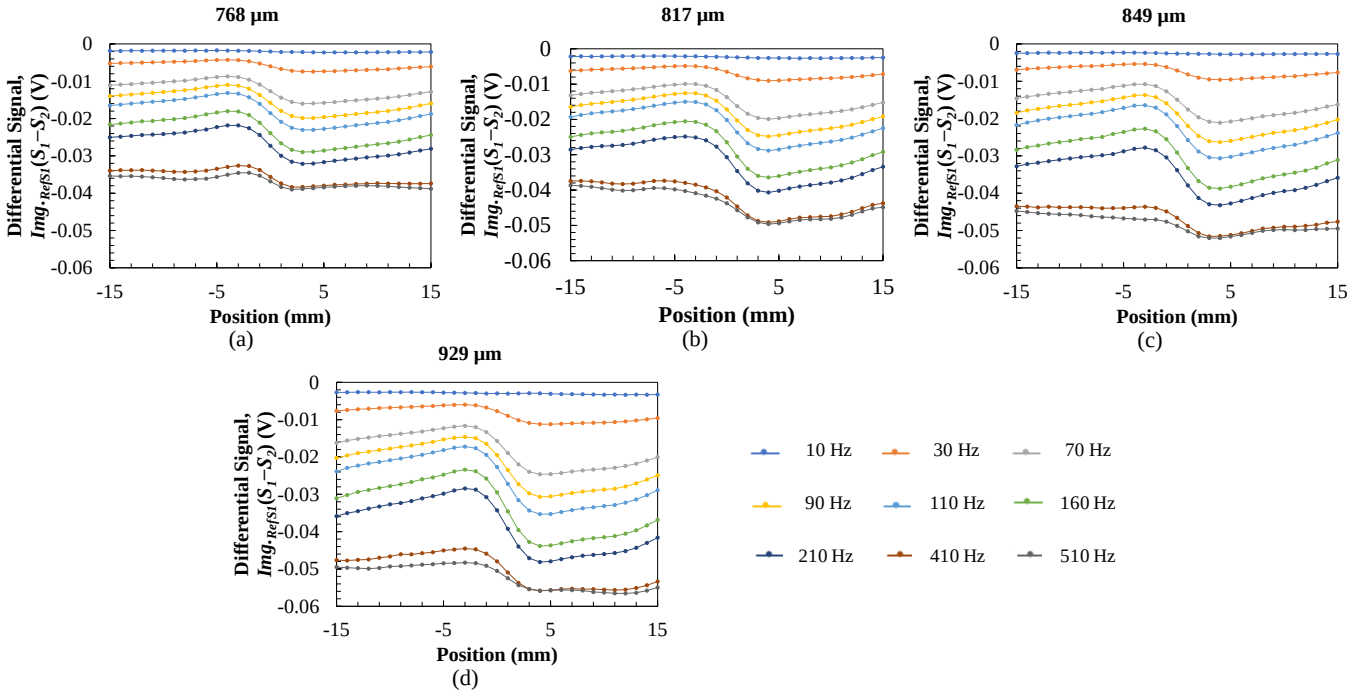

Figure 14 The waveforms of the measured imaginary components obtained from the differential signals of sensor 1 and sensor 2 using sensor 1 as the reference, $S_{1,RefS1}$-$S_{2,RefS1}$ at (a) 0.768-mm, (b) 0.817-mm (c) 0.849-mm and (d) 0.929-mm slits. The frequency was varied from 10 to 510 Hz and the sensor outputs were the B_z components and amplified by a gain of 129.

This article has been accepted for publication in a future issue of this journal, but has not been fully edited. Content may change prior to final publication. Citation information: DOI 10.1109/ACCESS.2021.3123421, IEEE Access

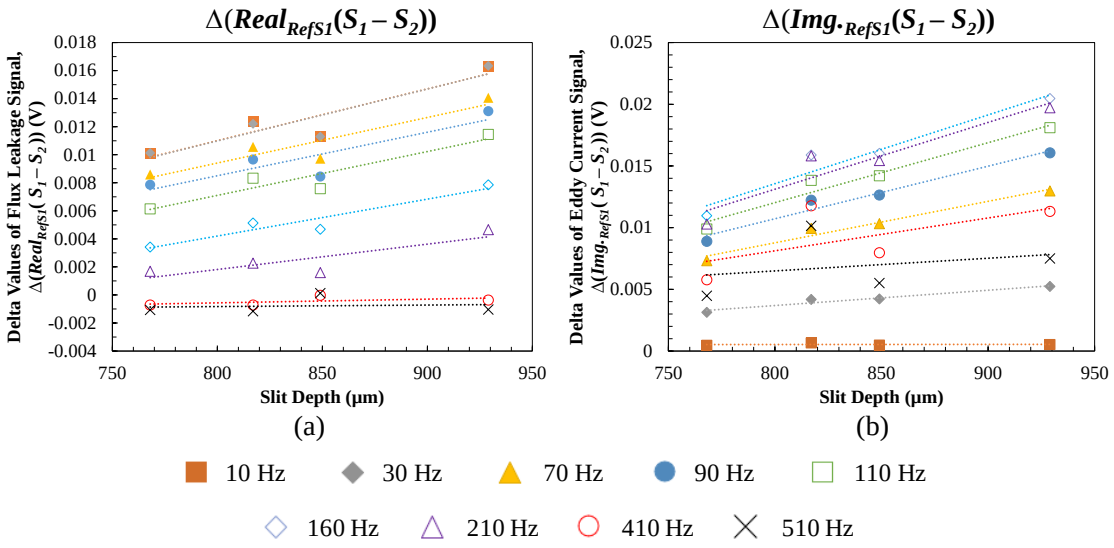

Figure 15 The delta values of both (a) magnetic flux leakage $\Delta(Real_{RefS1}(S_1\text{-}S_2))$ and (b) eddy current signals $\Delta(Img._{RefS1}(S_1\text{-}S_2))$ with frequency variation. A linear interpolation model was used to fit the data.

This article has been accepted for publication in a future issue of this journal, but has not been fully edited. Content may change prior to final publication. Citation information: DOI 10.1109/ACCESS.2021.3123421, IEEE Access

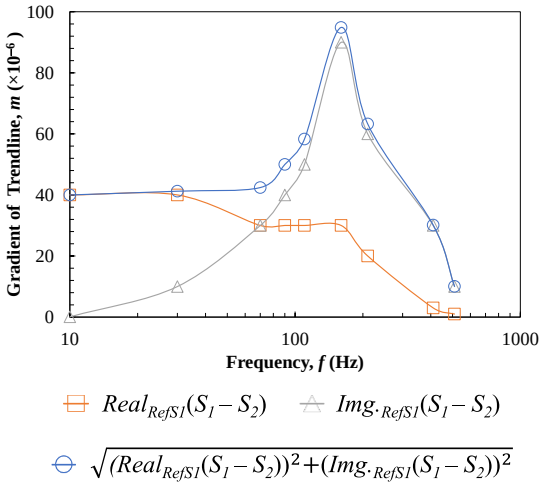

Figure 16 The gradient of the trendlines generated from the delta values in Fig. 15 versus frequency.

This article has been accepted for publication in a future issue of this journal, but has not been fully edited. Content may change prior to final publication. Citation information: DOI 10.1109/ACCESS.2021.3123421, IEEE Access

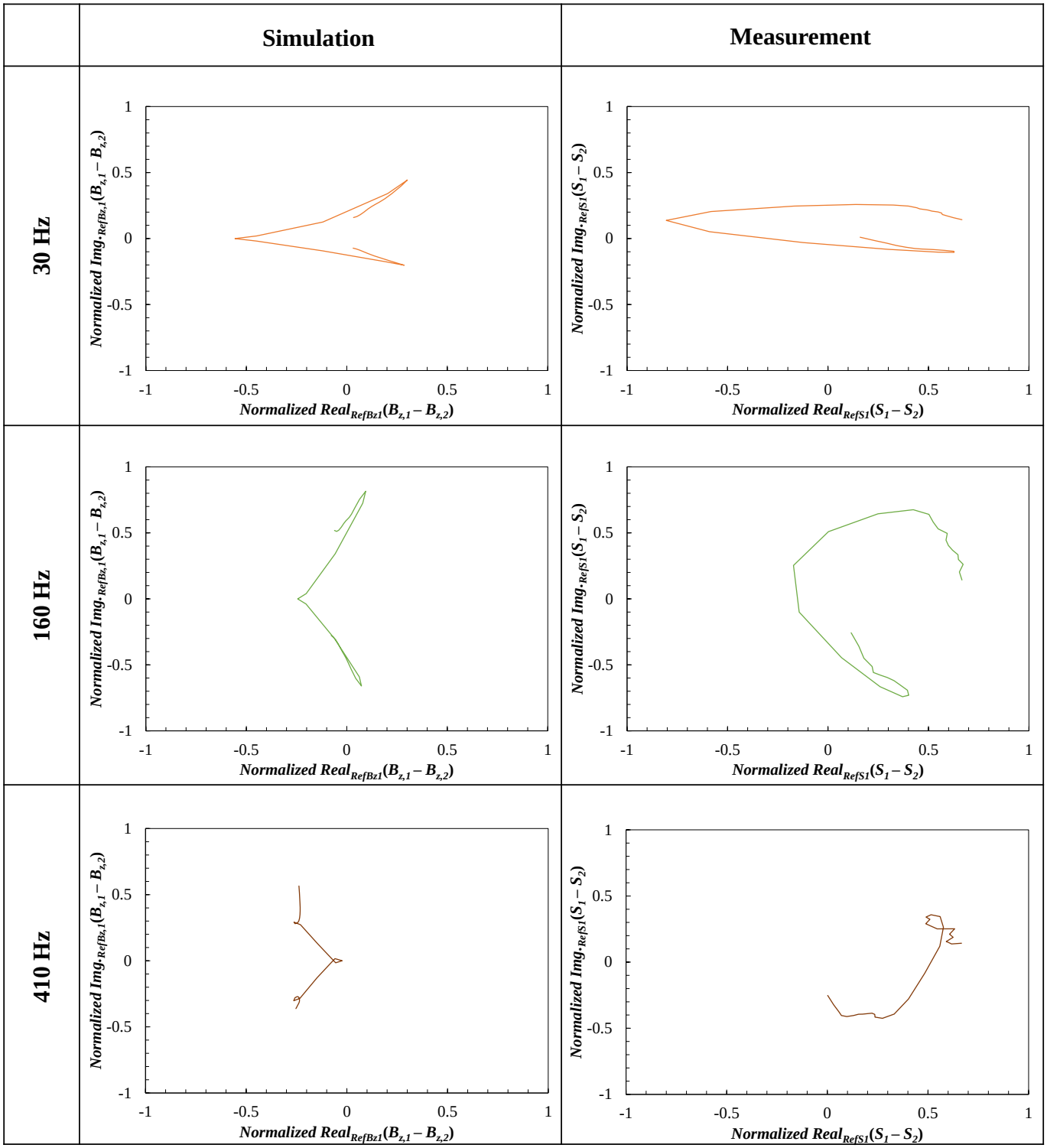

Figure 17 The Lissajous curves of the line scan measurements at the different excitation frequency of 30, 160 and 410 Hz conducted from the backside of the 2-mm sample. Slit depths of 1 and 0.929 mm were used in the simulation and measurement, respectively.

MOHD AUFA HADI PUTERA ZAINI received the B.Sc. degree (September 2014 to November 2018) and M.Sc degree (September 2018 to February 2021) in electrical electronics engineering from Universiti Malaysia Pahang, Pahang, Malaysia. He is currently pursuing the Ph.D. degree in instrumentation and control engineering at Universiti Malaysia Pahang. His research interest includes the application of electromagnetic method of NDT for the detection of defects such as crack and corrosion on metallic sample for both frontside and back-side detection.

MOHD MAWARDI SAARI (Member, IEEE) received the Bachelor of Engineering in electrical & electronic engineering (April 2007 to March 2011), Master of Engineering in electronic information system engineering (April 2011 to March 2013) and Doctor Philosophy of Engineering (April 2013 to September 2015) from Okayama University, Okayama, Japan. On January 2016, he joined Universiti Malaysia Pahang (UMP), Pahang, Malaysia, as a lecturer at Faculty of Electrical and Electronics Engineering Technology. He has been working on developing a highly sensitive DC magnetometer using high-Tc SQUID. He is currently working on developing an AC magnetometer for evaluation of magnetic nanoparticles and non-destructive test for defect evaluation in metal components.

NURUL A'IN NADZRI received the B.Sc. degree (September 2013 to November 2017) and M.Sc degree (September 2018 to November 2020) in electrical electronics engineering from Universiti Malaysia Pahang, Pahang, Malaysia. She is currently pursuing the Ph.D. degree in instrumentation and control engineering at Universiti Malaysia Pahang. Her research interest includes the application of electromagnetic method of NDT for the detection of defects such as crack and corrosion on metallic sample for both frontside and back-side detection

ZULKIFLY AZIZ received the B.Sc. degree in electrical and electronics engineering from Polytechnic University of Brooklyn New York (now New York University Tandon School of Engineering) in 1995, and M.Sc. degree in materials science in 2019 from Universiti Malaysia Pahang. He is currently pursuing the Ph.D. degree in instrumentation and control engineering under the faculty of electrical and electronics engineering technology at Universiti Malaysia Pahang. His research interest includes wireless power transfer, photocatalytic reforming, dye-sensitized solar cells, and biofeedback.

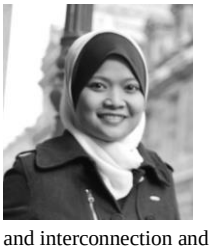

NUR HUDA RAMLAN received the Bachelor of Engineering in electrical & electronics (power systems) (2009) from Universiti Teknologi Petronas, Malaysia, Master Of Engineering in electrical power (2011) from Universiti Teknologi Malaysia, Malaysia, and Doctor Of Philosophy in electrical engineering (2017) from Universiti Teknologi Malaysia, Malaysia. Her main research interests include multilevel inverter and interconnection and damping assignment passivity based controller.

KEIJI TSUKADA received the Dr. Eng. and the PhD degrees from Tsukuba University in 1990, and 2001, respectively. He joined the Central Research Laboratory, Hitachi Ltd. in 1982, where he was involved in the study of integrated solid-state chemical sensor for blood analyses. He was with the Superconducting Sensor Laboratory from 1991 to 1996. He was involved in the research and development of SQUID's and multichannel SQUID system. He was with the Central Research Laboratory, Hitachi Ltd. from 1996 to 2003. He was a Project Leader of the SQUID application research group. He is presently an Emeritus Professor of Graduate School of Interdisciplinary Science and Engineering in Health Systems, Okayama University. He is involved in the research of non-destructive test, gas chemical sensor and superconducting sensor devices, and their applications.